ARL-RP-0518 • FEBRUARY 2015

US Army Research Laboratory

Phase Field Modeling of Directional Fracture in Anisotropic Polycrystals

by JD Clayton and J Knap

A reprint from Computational Materials Science, 2015;98:158–169.

Approved for public release; distribution unlimited.

NOTICES

Disclaimers

The findings in this report are not to be construed as an official Department of the Army position unless so designated by other authorized documents.

Citation of manufacturer’s or trade names does not constitute an official endorsement or approval of the use thereof.

Destroy this report when it is no longer needed. Do not return it to the originator.

ARL-RP-0518 ● FEBRUARY 2015

US Army Research Laboratory

Phase Field Modeling of Directional Fracture in Anisotropic Polycrystals

by JD Clayton
Weapons and Materials Research Directorate, ARL

and

J Knap
Computational and Information Sciences Directorate, ARL

A reprint from Computational Materials Science, 2015;98:158–169.

Approved for public release; distribution unlimited.

REPORT DOCUMENTATION PAGE

Form Approved
OMB No. 0704-0188

Public reporting burden for this collection of information is estimated to average 1 hour per response, including the time for reviewing instructions, searching existing data sources, gathering and maintaining the data needed, and completing and reviewing the collection information. Send comments regarding this burden estimate or any other aspect of this collection of information, including suggestions for reducing the burden, to Department of Defense, Washington Headquarters Services, Directorate for Information Operations and Reports (0704-0188), 1215 Jefferson Davis Highway, Suite 1204, Arlington, VA 22202-4302. Respondents should be aware that notwithstanding any other provision of law, no person shall be subject to any penalty for failing to comply with a collection of information if it does not display a currently valid OMB control number.

PLEASE DO NOT RETURN YOUR FORM TO THE ABOVE ADDRESS.

1. REPORT DATE *(DD-MM-YYYY)* February 2015	**2. REPORT TYPE** Final	**3. DATES COVERED (From - To)** January 2014–January 2015

4. TITLE AND SUBTITLE
Phase Field Modeling of Directional Fracture in Anisotropic Polycrystals

5a. CONTRACT NUMBER

5b. GRANT NUMBER

5c. PROGRAM ELEMENT NUMBER

6. AUTHOR(S)
JD Clayton and J Knap

5d. PROJECT NUMBER
AH80

5e. TASK NUMBER

5f. WORK UNIT NUMBER

7. PERFORMING ORGANIZATION NAME(S) AND ADDRESS(ES)
US Army Research Laboratory
ATTN: RDRL-WMP-C
Aberdeen Proving Ground, MD 21005-5066

8. PERFORMING ORGANIZATION REPORT NUMBER
ARL-RP-0518

9. SPONSORING/MONITORING AGENCY NAME(S) AND ADDRESS(ES)

10. SPONSOR/MONITOR'S ACRONYM(S)

11. SPONSOR/MONITOR'S REPORT NUMBER(S)

12. DISTRIBUTION/AVAILABILITY STATEMENT
Approved for public release; distribution unlimited

13. SUPPLEMENTARY NOTES
A reprint from Computational Materials Science, 2015;98:158–169.

14. ABSTRACT

A phase field theory for modeling deformation and fracture of single crystals, polycrystals, and grain boundaries is developed. Anisotropies of elastic coefficients and fracture surface energy are addressed, the latter enabling favorable cleavage on intrinsically weak planes in crystals. An order parameter increases in value as damage accumulates in an element of material. The shear elastic coefficients deteriorate with cumulative damage regardless of local strain state, while the effective bulk modulus degrades only under tensile volumetric deformation. Governing equations and boundary conditions are derived using variational methods. An incremental energy minimization approach is used to predict equilibrium crack morphologies in finite element simulations of deforming polycrystals. Thin layers of material, representative of glassy second phases near grain boundaries, are assigned possibly different properties than surrounding crystals. Results of simulations of polycrystals subjected to tensile loading are reported, with base properties representative of silicon carbide or zinc. Key findings include (i) a tendency for intergranular over transgranular fracture as the grain boundary surface energy is reduced or as cleavage anisotropy is increased and (ii) an increase in overall ductility and strength, the latter similar to Hall–Petch scaling, as the absolute size of the polycrystal is reduced while holding the ratio of phase field regularization length to grain size fixed.

15. SUBJECT TERMS
phase field, fracture, polycrystal, anisotropy, energy minimization

16. SECURITY CLASSIFICATION OF:			**17. LIMITATION OF ABSTRACT**	**18. NUMBER OF PAGES**	**19a. NAME OF RESPONSIBLE PERSON** J D Clayton
a. REPORT Unclassified	**b. ABSTRACT** Unclassified	**c. THIS PAGE** Unclassified	UU	18	**19b. TELEPHONE NUMBER (Include area code)** 410-278-6146

Standard Form 298 (Rev. 8/98)
Prescribed by ANSI Std. Z39.18

Computational Materials Science 98 (2015) 158–169

Contents lists available at ScienceDirect

Computational Materials Science

journal homepage: www.elsevier.com/locate/commatsci

Phase field modeling of directional fracture in anisotropic polycrystals

J.D. Clayton [a,*], J. Knap [b]

[a] Impact Physics RDRL-WMP-C, US Army Research Laboratory, Aberdeen Proving Ground, MD 21005-5066, USA
[b] Computational Sciences RDRL-CIH-C, US Army Research Laboratory, Aberdeen Proving Ground, MD 21005-5066, USA

ARTICLE INFO

Article history:
Received 25 August 2014
Received in revised form 31 October 2014
Accepted 4 November 2014

Keywords:
Phase field
Fracture
Polycrystal
Anisotropy
Energy minimization

ABSTRACT

A phase field theory for modeling deformation and fracture of single crystals, polycrystals, and grain boundaries is developed. Anisotropies of elastic coefficients and fracture surface energy are addressed, the latter enabling favorable cleavage on intrinsically weak planes in crystals. An order parameter increases in value as damage accumulates in an element of material. The shear elastic coefficients deteriorate with cumulative damage regardless of local strain state, while the effective bulk modulus degrades only under tensile volumetric deformation. Governing equations and boundary conditions are derived using variational methods. An incremental energy minimization approach is used to predict equilibrium crack morphologies in finite element simulations of deforming polycrystals. Thin layers of material, representative of glassy second phases near grain boundaries, are assigned possibly different properties than surrounding crystals. Results of simulations of polycrystals subjected to tensile loading are reported, with base properties representative of silicon carbide or zinc. Key findings include (i) a tendency for intergranular over transgranular fracture as the grain boundary surface energy is reduced or as cleavage anisotropy is increased and (ii) an increase in overall ductility and strength, the latter similar to Hall–Petch scaling, as the absolute size of the polycrystal is reduced while holding the ratio of phase field regularization length to grain size fixed.

Published by Elsevier B.V.

1. Introduction

Most structural applications of metals and ceramics involve polycrystalline forms of these materials. Mechanical properties such as hardness, strength, and ductility are often dominated by the grain structure: grain size and morphology, grain boundary character, lattice orientation, and defects which may segregate at boundaries or reside within crystals. Regarding grain size effects, a trend often observed in polycrystals is increasing strength with decreasing size (e.g., Hall–Petch strength increasing with the inverse square root of the grain size), which has been observed in metallic and ceramic solids with grains ranging from hundreds of microns to tens of nanometers in scale [1–3]. Mechanisms responsible for size versus strength scaling depend on the material and loading regime (e.g., competition among dislocation glide and grain boundary sliding in metals or weakest link or Weibull-type behavior in ceramics), and at extremely small grain sizes, the scaling relation holds less frequently, with a possible reversal in trend (inverse Hall–Petch behavior). Grain boundary interfaces more strongly affect properties as grain size is reduced: as the surface area to volume ratio of such interfaces increases, the relative volume fraction of material in close proximity to interfaces increases. In ceramics, grain boundaries are frequently the site of amorphous/glassy phases of material whose properties differ from surrounding crystals [2,4–6].

Continuum polycrystal models, wherein individual crystals are resolved numerically, are useful for probing possible relationships among microstructure features and mechanical response. Perhaps most often used in the previous two decades for modeling fracture are cohesive finite element approaches. Applications to ceramics include [4,7–9]; applications to metals include [10,11]. These models have advantages of flexibility of user-prescribed cohesive laws and have been successful for describing many effects of microstructure on failure. However, crack paths follow mesh boundaries so mesh construction cannot be arbitrary; three-dimensional modeling of fracture in complex microstructures using the cohesive finite element method is difficult and computationally expensive. Other two-dimensional computational approaches applied towards modeling polycrystalline deformation and fracture include the extended finite element method (XFEM) [12] and the cohesive boundary element method [13]; in three dimensions, continuum viscoplastic modeling of grain boundary phases of finite thickness has also been undertaken [14].

---

* Corresponding author.
E-mail addresses: john.d.clayton1.civ@mail.mil (J.D. Clayton), jaroslaw.knap.civ@mail.mil (J. Knap).

http://dx.doi.org/10.1016/j.commatsci.2014.11.009
0927-0256/Published by Elsevier B.V.

An alternative approach is invoked in the present work: the phase field method. Phase field theory has been applied towards a wide range of physical problems involving changes in structure or representation of crystal defects: phase transitions [15], dislocations [16,17], void growth [18], twinning [19–23], and amorphization [24]. Some relevant phase field models of fracture developed elsewhere include [25–33]. These models typically require kinetic parameters to describe the rate of damage/crack propagation, e.g., as in the Ginzburg–Landau equations, Allen–Cahn equations, or similar rate equations. In contrast, the present work seeks equilibrium solutions of the governing equations of momentum and order parameter distribution via incremental energy minimization, as also explained in [34]. The only material parameters needed in the present theory are the crack plane normal (for anisotropic fracture), surface energy of fracture, and elastic constants. A numerical parameter is also needed for regularization such that the minimum crack width is at least of the order of the mesh size. Earlier works incorporating variational approaches to modeling brittle fracture with some features in common with the present theory include [35–37]. The phase field description of fracture should be contrasted with continuum damage mechanics descriptions such as [38,39] that do not explicitly incorporate an intrinsic length scale for regularization.

A geometrically nonlinear theory with anisotropic fracture energy but isotropic elasticity was recently developed in [34]. This theory was merged/coupled with a nonlinear phase field theory for twinning, and solutions were analyzed for finite simple shear deformation, in [40]. The present model, although linear elastic, appears to be one of the first for modeling effects of simultaneous anisotropic fracture energy and anisotropic elasticity in polycrystals, the latter not considered in [34,40]. Phase field modeling of polycrystals with grain boundary regions whose properties may differ from surrounding crystals, similar to the present implementation, was reported in [31], in work that considered isotropic fracture energy, anisotropic elasticity, electromechanical coupling, and a kinetic approach to evolution of order parameter fields. In that work, all grain sizes were in the nanometer regime, and all numerical simulations were two-dimensional. A transition from intergranular to transgranular failure was found as the grain size was increased, in conjunction with an increase in overall fracture toughness. In contrast, newly reported here are effects of anisotropic cleavage properties within crystals, large variations in grain size/resolution spanning nanoscale to microscale, and various grain boundary properties, all in the context of three-dimensional simulations invoking incremental energy minimization (quasi-statics). The present focus is on two materials: hexagonal polytypes of silicon carbide (SiC) and zinc (Zn), both of whose most likely transgranular fracture surfaces have been reported as the basal plane [41,42]. Increases in hardness or strength have been reported for polycrystals of these materials as their grain sizes decrease to ultra-fine (several hundred nm to micron) and nanometer scales [5,6,43,44].

An outline of the remainder of this paper is as follows. The phase field theory is described in Section 2. Numerical implementation using the finite element method, along with representative material properties for SiC and Zn and numerical representation of their polycrystalline structures, are discussed in Section 3. Results of phase field simulations are reported in Section 4, wherein relative importance of model parameters and microstructure aspects on mechanical response are deduced. Conclusions follow in Section 5. Standard notation of modern continuum field theory is used: vectors and tensors in bold italic font, scalars and components in italic font. Summation applies over repeated indices when the index notation is invoked, with components referred to a fixed Cartesian frame of reference.

2. Phase field theory

First, governing equations are derived in the context of small strain theory, but without reference to any specific strain energy function. Next, anisotropic and isotropic elasticity models are described.

2.1. Governing equations

Let $\boldsymbol{x}$ denote coordinates occupied by a material body Ω and let t denote time. Let $\xi(\boldsymbol{x},t)$ denote the order parameter associated with fracture:

$$\begin{aligned}&\xi = 0\,\forall\boldsymbol{x}\in \text{solid},\\ &\xi = 1\,\forall\boldsymbol{x}\in \text{failed domain},\\ &\xi \in (0,1)\,\forall\boldsymbol{x}\in \text{cohesive boundary}.\end{aligned} \tag{2.1}$$

Denote by $\boldsymbol{u}(\boldsymbol{x},t)$ the displacement. The displacement gradient is $\nabla\boldsymbol{u}$. Define the symmetric linear strain tensor and its trace quantifying local volume change:

$$\boldsymbol{\varepsilon} = \frac{1}{2}[\nabla\boldsymbol{u} + (\nabla\boldsymbol{u})^{\mathrm{T}}], \qquad \mathrm{tr}\boldsymbol{\varepsilon} = \nabla\cdot\boldsymbol{u}. \tag{2.2}$$

The total energy functional for the body is

$$\Psi(\boldsymbol{u},\xi) = \int_{\Omega}[W(\nabla\boldsymbol{u},\xi) + g(\xi,\nabla\xi)]\mathrm{d}\Omega. \tag{2.3}$$

Strain energy per unit volume W is of the general form

$$W = W[\boldsymbol{\varepsilon}(\nabla\boldsymbol{u}),\xi]. \tag{2.4}$$

Interfacial energy per unit volume is of the general form

$$g = g_0(\xi) + \boldsymbol{\omega} : (\nabla\xi\otimes\nabla\xi), \tag{2.5}$$

where $\boldsymbol{\omega}$ is a symmetric second-order tensor. Consider a simply connected body of volume Ω with external boundary $S = \partial\Omega$. Imposing the variational principle

$$\delta\Psi = \oint_{\partial\Omega}(\boldsymbol{t}\cdot\delta\boldsymbol{u} + s\delta\xi)\mathrm{d}S, \tag{2.6}$$

and assuming fields are sufficiently smooth, the following local equilibrium equations in Ω and boundary conditions on $\partial\Omega$ are derived, following general methods outlined for example in [19,40]:

$$\nabla\cdot\left.\frac{\partial W}{\partial\nabla\boldsymbol{u}}\right|_{\xi} = \nabla\cdot\boldsymbol{P} = 0; \tag{2.7}$$

$$\frac{\partial g}{\partial\xi} - 2\nabla\cdot(\boldsymbol{\omega}\nabla\xi) + \left.\frac{\partial W}{\partial\xi}\right|_{\nabla\boldsymbol{u}} = 0; \tag{2.8}$$

$$\boldsymbol{t} = \boldsymbol{P}\cdot\boldsymbol{n}, \qquad s = 2\boldsymbol{\omega} : (\nabla\xi\otimes\boldsymbol{n}). \tag{2.9}$$

The traction vector (mechanical force per unit area) on $\partial\Omega$ is $\boldsymbol{t}$; the scalar conjugate force to order parameter ξ on $\partial\Omega$ is s; the outward unit normal vector to $\partial\Omega$ is $\boldsymbol{n}$. The symmetric stress tensor is

$$\boldsymbol{P} = \frac{\partial W}{\partial\nabla\boldsymbol{u}} = \frac{\partial W}{\partial\boldsymbol{\varepsilon}}. \tag{2.10}$$

The elastic driving force for fracture is the scalar

$$\varsigma = \partial W(\nabla\boldsymbol{u},\xi)/\partial\xi. \tag{2.11}$$

For cleavage fracture on a preferred plane, it is assumed that the orientation of such a plane is known a priori. For example, this would be a plane or family planes of low surface energy or low intrinsic strength in a crystal. Considered herein is a single orientation. The unit vector (in material coordinates) normal to this potentially preferred cleavage plane is $\boldsymbol{M}$. Let B, ω_0, and χ denote constants. For the present fracture model,

$$g_0(\xi) = B\xi^2, \qquad \boldsymbol{\omega} = \omega_0[\mathbf{1} + \beta(\mathbf{1} - \boldsymbol{M} \otimes \boldsymbol{M})]. \tag{2.12}$$

Crack thickness l (i.e., phase field regularization width) and nominal surface energy per unit area Γ are related as [28,34,40]

$$B = \Gamma / l, \qquad \omega_0 = \Gamma l. \tag{2.13}$$

Setting $\beta \gg 0$ penalizes fracture on planes not normal to $\boldsymbol{M}$. Setting $\beta = 0$ results in isotropic damage when used with isotropic modulus degradation. Substituting from (2.12), the Euler–Lagrange equation for order parameter equilibrium in (2.8) becomes

$$\varsigma = 2\omega_0[\nabla^2\xi + \beta(\nabla^2\xi - \boldsymbol{M} \otimes \boldsymbol{M} : \nabla\nabla\ \xi)] - 2B\xi. \tag{2.14}$$

Note that in the present variational approach, time t does not enter the governing equations and can be regarded as a simple load parameter in the context of incrementally updated boundary conditions, for example.

As described later in Sections 3 and 4, the present theory is applied towards computational modeling of polycrystalline fracture. Polycrystals are represented by collections of discrete polyhedral grains of varying initial lattice orientations, with possible secondary glassy phases in between. Elasticity of each grain is generally anisotropic, while all properties of glassy phases are considered isotropic. Fractures within each grain are generally anisotropic, with a preference for planar/flat fractures along planes with unit normal $\boldsymbol{M}$ which is constant within each single crystal. The larger the value of penalty factor β, the greater the tendency for planar cleavage fracture. In contrast, as $\beta \to 0$, the fracture model tends towards isotropy, and curved or conchoidal fracture surfaces become more feasible.

The present theory can be applied immediately to computational modeling of single crystals by omitting grain boundaries and grain boundary phases and assigning uniform material properties (i.e., lattice orientation-dependent elastic constants and surface energy) throughout the entire simulation domain. The present implementation is restricted to crystals with a single dominant cleavage plane (e.g., $\boldsymbol{M}$ corresponding to basal plane fracture in hexagonal/HCP crystals). A conceivable method of extension of the theory to consider preferential fracture on cleavage planes of multiple discrete orientations requires introduction of additional order parameter(s) for quantification of damage accumulation and failure on each such plane.

2.2. Anisotropic elasticity

The elasticity tensor (i.e., tangent elastic modulus) $\mathbf{C}$ depends on the order parameter, and more specifically is degraded upon fracture, as detailed below. Let $\mathbf{C}^0$ denote the elasticity tensor of the perfect material:

$$\mathsf{C}^0_{IJKL} = \mathsf{C}_{IJKL}|_{\xi=0} = \left.\frac{\partial^2 W}{\partial \varepsilon_{IJ} \varepsilon_{KL}}\right|_{\xi=0}. \tag{2.15}$$

Bulk modulus k_0 for the undamaged material is defined as usual for crystals of cubic, hexagonal, or trigonal symmetry [45,46]:

$$k_0 = \frac{(\mathsf{C}_{11} + \mathsf{C}_{12})\mathsf{C}_{33} - 2\mathsf{C}_{13}^2}{\mathsf{C}_{11} + \mathsf{C}_{12} + 2\mathsf{C}_{33} - 4\mathsf{C}_{13}}. \tag{2.16}$$

where $\mathsf{C}_{\alpha\beta} \leftrightarrow \mathsf{C}^0_{IJKL}$ are initial/undamaged elastic constants in Voigt notation (Greek indices running from 1 to 6). For linear anisotropic elastic response, the strain energy potential is defined as the quadratic form in strain

$$W = \frac{1}{2}\boldsymbol{\varepsilon} : \mathbf{C}(\xi, \nabla \cdot \boldsymbol{u}) : \boldsymbol{\varepsilon}. \tag{2.17}$$

The tangent elasticity tensor depends on ξ and possibly volume change:

$$\mathsf{C}_{IJKL} = \mathsf{C}^0_{IJKL}[\zeta + (1-\zeta)(1-\xi)^2] + k_0\delta_{IJ}\delta_{KL}[1 - \zeta - (1 - \zeta)(1-\xi)^2]\langle -\nabla \cdot \boldsymbol{u}\rangle^*. \tag{2.18}$$

Here, $\zeta \in [0, 1)$ is a constant of usual magnitude much less than unity that is used to provide some residual elastic stiffness in damaged regions where $\xi \to 1$; increasing this parameter has been found to improve numerical stability in some cases. The following notation applies: $\langle x \rangle = 1 \forall x > 0$, $\langle x \rangle = 0 \forall x \leqslant 0$, $\langle x \rangle^* = 1 \forall x \geqslant 0$, and $\langle x \rangle^* = 0 \forall x < 0$. The present model permits degradation of the bulk modulus only when volume change is tensile and degradation of the shear modulus regardless of whether loading is tensile or compressive. In compression, the elasticity tensor ultimately degrades to isotropic elasticity with the bulk modulus held fixed and shear moduli decreased by a factor of ζ. This approach is the anisotropic analog to that implemented in the isotropic linear elastic phase field theory of [47].

The following partial derivatives are used in governing equations and subsequent numerical implementation of the theory:

$$\boldsymbol{P} = \left.\frac{\partial W}{\partial \nabla \boldsymbol{u}}\right|_{\xi} = \mathbf{C}(\xi, \nabla \cdot \boldsymbol{u}) : \boldsymbol{\varepsilon} + \frac{1}{2}\left[\boldsymbol{\varepsilon} : \frac{\partial \mathbf{C}}{\partial(\nabla \cdot \boldsymbol{u})} : \boldsymbol{\varepsilon}\right]\mathbf{1} \approx \mathbf{C} : \boldsymbol{\varepsilon}, \tag{2.19}$$

$$\left.\frac{\partial^2 W}{\partial \nabla_J u_I \partial \nabla_L u_K}\right|_{\xi} \approx \mathsf{C}_{IJKL}; \tag{2.20}$$

$$\varsigma = \left.\frac{\partial W}{\partial \xi}\right|_{\nabla \boldsymbol{u}} = \frac{1}{2}\left[\boldsymbol{\varepsilon} : \frac{\partial \mathbf{C}}{\partial \xi} : \boldsymbol{\varepsilon}\right], \tag{2.21}$$

$$\frac{\partial \mathsf{C}_{IJKL}}{\partial \xi} = [-2\mathsf{C}^0_{IJKL}(1-\xi) + 2k_0\delta_{IJ}\delta_{KL}(1-\xi)\langle -\nabla \cdot \boldsymbol{u}\rangle^*](1-\zeta); \tag{2.22}$$

$$\frac{\partial \varsigma}{\partial \xi} = \left.\frac{\partial^2 W}{\partial \xi^2}\right|_{\nabla \boldsymbol{u}} = \frac{1}{2}\left[\boldsymbol{\varepsilon} : \frac{\partial^2 \mathbf{C}}{\partial \xi^2} : \boldsymbol{\varepsilon}\right], \tag{2.23}$$

$$\frac{\partial^2 \mathsf{C}_{IJKL}}{\partial \xi^2} = [2\mathsf{C}^0_{IJKL} - 2k_0\delta_{IJ}\delta_{KL}\langle -\nabla \cdot \boldsymbol{u}\rangle^*](1-\zeta); \tag{2.24}$$

$$\frac{\partial g}{\partial \xi} = 2B\xi, \qquad \frac{\partial^2 g}{\partial \xi^2} = 2B; \tag{2.25}$$

$$\frac{\partial g}{\partial \nabla \xi} = 2\boldsymbol{\omega}\nabla\xi, \qquad \frac{\partial^2 g}{\partial \nabla\xi \partial \nabla\xi} = 2\boldsymbol{\omega}. \tag{2.26}$$

Approximations in (2.19) and (2.20) omit the singularity associated with tension–compression asymmetry in the bulk modulus arising at $\nabla \cdot \boldsymbol{u} = 0$ when $\xi > 0$.

A phase field theory for twinning incorporating nonlinear anisotropic elasticity was developed in [19] involving an elastic potential with Green–Lagrange strain, the conventional finite strain measure encountered in nonlinear elasticity of crystals [48]. However, numerical results could not be obtained due to intrinsic instabilities which can be artifacts of such constitutive models in compression [45,49]. Extension of the phase field fracture model to nonlinear anisotropic elasticity may proceed in the future with Eulerian material strain [50] or logarithmic strain [46] which tend to provide more accurate and stable results for crystals under finite compression and shear. Other avenues for extension to account for ductile fracture involving plasticity include incorporation of order parameters for dislocation dynamics [17] and residual dilatation fields of dislocations [51].

2.3. Isotropic elasticity

For completeness, isotropic linear elasticity is now considered, where the strain energy potential is

$$W[\boldsymbol{\varepsilon}(\nabla \boldsymbol{u}), \xi] = \frac{1}{2}\lambda(\mathrm{tr}\boldsymbol{\varepsilon})^2 + \mu\boldsymbol{\varepsilon} : \boldsymbol{\varepsilon}. \tag{2.27}$$

Lamé coefficients μ and λ depend on ξ and possibly volume change [34,47]:

$$\mu(\xi) = \mu_0[\zeta + (1-\zeta)(1-\xi)^2], \qquad \lambda = k(\xi, \nabla\cdot\boldsymbol{u}) - \frac{2}{3}\mu(\xi); \tag{2.28}$$

$$k = (\lambda_0 + \frac{2}{3}\mu_0)\{[\zeta + (1-\zeta)(1-\xi)^2]\langle\nabla\cdot\boldsymbol{u}\rangle + \langle -\nabla\cdot\boldsymbol{u}\rangle^*\}. \tag{2.29}$$

Eqs. (2.12), (2.13), (2.25), and (2.26) still hold. The additional partial derivatives below are used in Euler–Lagrange equations and numerical implementation:

$$\boldsymbol{P} = \left.\frac{\partial W}{\partial\nabla\boldsymbol{u}}\right|_{\xi} = \lambda(\mathrm{tr}\boldsymbol{\varepsilon})\mathbf{1} + 2\mu\boldsymbol{\varepsilon} + \frac{1}{2}\lambda(\mathrm{tr}\boldsymbol{\varepsilon})^2\frac{\partial k}{\partial(\nabla\cdot\boldsymbol{u})}\mathbf{1} \approx \lambda(\nabla\cdot\boldsymbol{u})\mathbf{1} + 2\mu\boldsymbol{\varepsilon}, \tag{2.30}$$

$$\left.\frac{\partial^2 W}{\partial\nabla_J u_I \partial\nabla_L u_K}\right|_{\xi} \approx \lambda\delta_{IJ}\delta_{KL} + \mu(\delta_{IK}\delta_{JL} + \delta_{IL}\delta_{JK}); \tag{2.31}$$

$$\varsigma = \left.\frac{\partial W}{\partial\xi}\right|_{\nabla\boldsymbol{u}} = \frac{1}{2}\left(\frac{\partial k}{\partial\xi} - \frac{2}{3}\frac{\partial\mu}{\partial\xi}\right)(\nabla\cdot\boldsymbol{u})^2 + \frac{\partial\mu}{\partial\xi}\boldsymbol{\varepsilon}:\boldsymbol{\varepsilon}, \tag{2.32}$$

$$\frac{\partial k}{\partial\xi} = -2(\lambda_0 + \frac{2}{3}\mu_0)\{[(1-\zeta)(1-\xi)]\langle\nabla\cdot\boldsymbol{u}\rangle\}, \quad \frac{\partial\mu}{\partial\xi} = -2\mu_0(1-\zeta)(1-\xi); \tag{2.33}$$

$$\frac{\partial\varsigma}{\partial\xi} = \left.\frac{\partial^2 W}{\partial\xi^2}\right|_{\nabla\boldsymbol{u}} = \frac{1}{2}\left(\frac{\partial^2 k}{\partial\xi^2} - \frac{2}{3}\frac{\partial^2\mu}{\partial\xi^2}\right)(\nabla\cdot\boldsymbol{u})^2 + \frac{\partial^2\mu}{\partial\xi^2}\boldsymbol{\varepsilon}:\boldsymbol{\varepsilon}, \tag{2.34}$$

$$\frac{\partial^2 k}{\partial\xi^2} = 2(\lambda_0 + \frac{2}{3}\mu_0)[(1-\zeta)\langle\nabla\cdot\boldsymbol{u}\rangle], \quad \frac{\partial^2\mu}{\partial\xi^2} = 2\mu_0(1-\zeta). \tag{2.35}$$

Using first derivatives above, the Euler–Lagrange equation for order parameter equilibrium is identical in form to (2.14); driving forces on left sides differ for anisotropic and isotropic elasticity, respectively given in (2.21) and (2.32).

3. Finite element modeling

An overview of implementation and application of the anisotropic phase field theory of Section 2 towards polycrystalline microstructures follows next. Discussed in turn are numerical methods for solution of governing equations, material properties, and representations of polycrystalline microstructures via Lagrangian finite elements.

3.1. Numerical methods

Complex two- and three-dimensional boundary value problems require numerical solutions, which are found here incrementally using the finite element method, for example via general procedures outlined in [19], wherein boundary conditions for displacement and order parameter (or their conjugate forces) are updated during each load increment. Nodal degrees of freedom are displacement $\boldsymbol{u}$ and order parameter ξ. For certain boundary conditions, candidate solutions [i.e., fields $\boldsymbol{u}(\boldsymbol{x}), \xi(\boldsymbol{x})$] are obtained that minimize $\Psi(\boldsymbol{u}, \xi)$ and thus satisfy (2.6). However, because Ψ is generally non-convex, multiple (local) minima may exist, and therefore solutions may be non-unique; when Ψ of such a local minima exceeds the global minimum energy, then such a solution is said to be metastable. Second derivatives listed in Sections 2.2 and 2.3 (e.g., tangent moduli) are intended for use in finding numerical solutions via conjugate gradient energy minimization. To ensure irreversibility of crack extension, the local internal constraint $\delta\xi(\boldsymbol{x}) \geqslant 0$ for $\xi(\boldsymbol{x}) \geqslant \xi_T$, with ξ_T some threshold value, is imposed [36,34]. Here, as in [36], the value $\xi_T = 0.9$ is used. If the above irreversibility constraint on $\delta\xi$ is not enforced, then fracture becomes thermodynamically reversible and cracks will heal fully upon unloading, a feature noted in other phase field implementations [26].

In the current implementation of the phase field theory, cracks represented by positive values of order parameter ξ are predicted to follow paths dictated by incremental total energy minimization, subject to the irreversibility constraint described above. When this constraint is active, the incremental energy minimization problem can be viewed as minimization of energy of an alternative system with time dependent boundary conditions associated with introduction of new (free) surfaces along which $\xi \geqslant 0.9$ is prescribed; equilibrium Eqs. (2.7) and (2.8) remain satisfied in solutions thus obtained for this alternative system.

3.2. Materials

Two representative anisotropic crystalline solids are considered in this paper, one ceramic (SiC) and one metallic (Zn), both with hexagonal crystal structures. Cleavage fracture planes in each kind of crystal have been reported as the basal plane [41,42], or (0001) in hexagonal Miller indices. Properties for SiC are listed in Table 1, applicable at room temperature conditions wherein the ceramic is inherently brittle. Various polytypes of SiC exist that may have hexagonal, cubic, or trigonal crystal structures; tabulated properties are most applicable to the hexagonal 6H polytype [52]. Typical grain sizes are on the order of tens of microns, but polycrystals with grains as small as 5–15 nm have been reported [6], with glassy interphase boundaries observed frequently in this nanocrystalline SiC. Increasing hardness and decreasing elastic stiffness with decreasing grain size and increasing volume fraction of amorphous grain boundary phase have been noted [6]. Properties for Zn are listed in Table 2, applicable at low temperature conditions (77 K) wherein the metal becomes brittle due to reduced mobility of gliding dislocations and twinning partial dislocations. In Zn, an increase in strength and decrease in ductility have been observed as grain sizes are reduced from hundreds of microns to tens of nanometers [43,44]. Peak ductility has been noted for the ultra-fine grained regime (grain sizes of several hundred nm), wherein grain boundary sliding has been posited as a likely primary deformation mechanism [44].

For each material, in addition to the five independent second-order anisotropic elastic constants, the bulk modulus k_0 obtained from (2.16) and the Voigt-averaged shear modulus μ_0 are also listed in Tables 1 and 2. These isotropic constants are used as base stiffness values for amorphous grain boundary regions in many simulations. Grain boundary phases are assigned isotropic fracture properties ($\beta = 0$) with surface energy Γ_G whose value is varied among simulations. The following ratios of grain boundary to bulk surface energy and elastic shear stiffness are also defined, where the G subscript refers to a property value used for the isotropic grain boundary region:

Table 1
Room temperature properties of silicon carbide.

Parameter	Value	Definition	Reference
C_{11}	501	Elastic constants (300 K) [GPa]	[52]
C_{12}	112		
C_{13}	52		
C_{33}	549		
C_{44}	161		
k_0	222	Bulk modulus [GPa]	
μ_0	192	Shear modulus [GPa]	
R_μ	0.1–10	Relative elastic stiffness of grain boundary phase	
Γ	860	Cleavage energy [mJ/m^2]	[52]
R_Γ	0.1–10	Relative surface energy of grain boundary phase	
β	0–100	Cleavage anisotropy	[34]
ζ	10^{-4}–10^{-2}	Residual stiffness	[34,36]
L	10^{-1}–10^{2}	Domain size [μm]	
l/L	10^{-2}	Ratio of regularization width to domain size	[47]

Table 2
Low temperature properties of zinc.

Parameter	Value	Definition	Reference
C_{11}	17.4	Elastic constants (77 K) [GPa]	[53]
C_{12}	3.4		
C_{13}	5.1		
C_{33}	6.7		
C_{44}	4.5		
k_0	6.3	Bulk modulus [GPa]	
μ_0	5.1	Shear modulus [GPa]	
R_μ	1	Relative elastic stiffness of grain boundary phase	
Γ	105	Cleavage energy [mJ/m^2]	[42,54]
R_Γ	1	Surface energy of grain boundary phase	
β	100	Cleavage anisotropy	[34]
ζ	10^{-2}	Residual stiffness	[34]
L	10^{-1}–10^{2}	Domain size [μm]	
l/L	10^{-2}	Ratio of regularization width to domain size	[47]

$$R_\Gamma = \Gamma_G/\Gamma, \qquad R_\mu = (\mu_0)_G/\mu_0 = (k_0)_G/k_0. \tag{3.1}$$

Effects of various prescriptions of residual elastic stiffness factor ζ are also examined, where $\zeta \gtrsim 10^{-4}$ was found necessary for numerical stability. Regularization parameter l is varied among simulations of SiC and Zn that consider domains with mesh dimensions of various scales, subject to resolution constraints that require l to be on the order of the mesh size or larger [19,30,34], leading to the fixed values of l/L shown in Tables 1 and 2.

3.3. Polycrystalline representations

Synthetic microstructures representative of generic polycrystals with equi-axed grains are considered in the present work, in the absence of serial section and/or electron back-scatter diffraction (EBSD) data that could be used to recreate true microstructures from material specimens [55]. First consider microstructures in which grain boundary phases are absent. In the present approach, identical to that taken in [9], volume meshes are created from stereolithographic (STL) files of surface representations of grains comprising a given microstructure. Surface meshes are generated for three-dimensional microstructures produced using a Monte Carlo grain growth algorithm [56]. A conformal triangular surface mesh covers each crystal volume, with an interpolation method used where a triangle separates two materials [57]. A three-dimensional volume mesh of hexahedral continuum finite elements is then created to fill the surface mesh of every crystal.

Most simulations feature polycrystals with amorphous grain boundary phases. For these simulations, the original microstructure without such phases is remeshed uniformly with hexahedral elements of constant size. Elements whose centroids lie within distance $w/2$ of any grain boundary surface are then reassigned from a crystal to the amorphous phase.

The polycrystalline microstructure consists of 50 grains. This aggregate is a cube of dimensions $L \times L \times L$, with one corner fixed

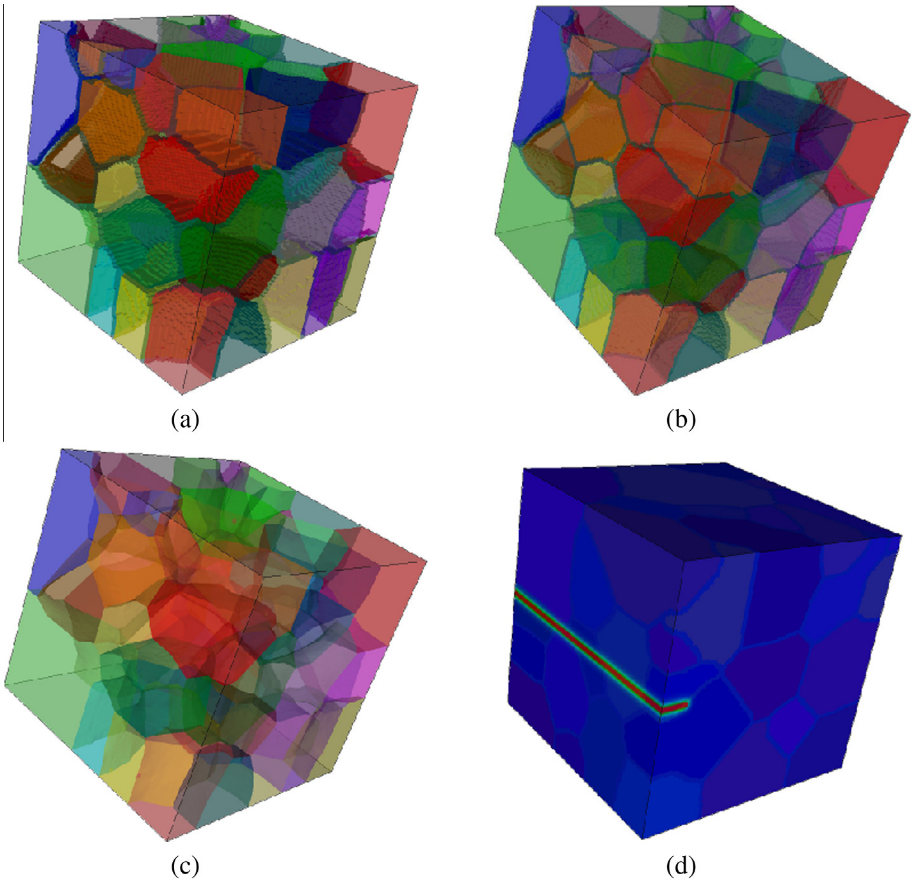
(a)
(b)
(c)
(d)

Fig. 1. Polycrystalline microstructures: (a) microstructure 1; (b) microstructure 2; (c) microstructure 3; (d) initial edge crack [self-equilibrated order parameter contour at null applied strain ($\varepsilon = 0$); red $\leftrightarrow \xi = 1$; blue $\leftrightarrow \xi = 0$]. (For interpretation of the references to colour in this figure legend, the reader is referred to the web version of this article.)

Table 3
Polycrystalline microstructures.

Microstructure	GB fraction, υ	GB thickness, w/L
1	0.202	0.020
2	0.139	0.013
3	0.000	0.000

at $(x,y,z) = (0,0,0)$ and the opposite corner at $(x,y,z) = (L,L,L)$. Microstructures are shown in Fig. 1. Average grain sizes for each microstructure can be estimated as $d \approx L/50^{1/3} \approx L/4$. Use of the same meshes for each material enables quantification of differences in deformation and failure behavior by varying material properties (i.e., elasticity, surface energy) while holding the microstructure fixed. Differences resulting from grain morphology are studied by deforming each microstructure in different directions. Finite element meshes contain between 1×10^6 and 3.5×10^6 hexahedral elements. Mesh refinement is sufficient to resolve grain boundary surface morphology and fracture regularization length l. Three meshes are considered, labeled microstructures 1, 2, and 3 in Table 3, and shown in Fig. 1(a)–(c). Microstructures 1 and 2 contain amorphous grain boundary phase of volume fraction υ and may fracture along grain boundaries and/or through grains. Microstructure 3 is fully crystalline (no second phase), with perfectly bonded grains, essentially restricting fractures to transgranular type, though stress concentrations from anisotropic elastic coefficient mismatch at grain boundaries may affect damage initiation and evolution.

In all simulations discussed in Section 4, random initial lattice orientations are used for grains comprising each microstructure. Different sets of random initial orientations are investigated in some simulations. Lattice orientation affects model results through the dependence of anisotropic elastic coefficients $C_{\alpha\beta}$ and direction of normal to the cleavage (basal) plane $\boldsymbol{M}$ on crystallographic orientation. Absolute sizes of each mesh are varied in the range 10^2 nm $\leqslant L \leqslant 10^5$ nm among simulations reported in Section 4, leading to approximate grain sizes d ranging from 25 nm to 25 μm.

Further remarks on the resolution of grain boundaries are in order. A grain boundary is considered fully coherent when lattices on either side match perfectly; for example, coherent boundaries contain no dislocations or vacancies associated with respective shear or volumetric incompatibility at the interface [58,59]. Fully incoherent grain boundaries demonstrate a highly disordered (lack of) structure, with the possibility of a large density of lattice defects. Semi-coherent boundaries consist of local regions wherein lattices match, interspersed with regions of mismatch and possible defects. Perfect twin boundaries may be categorized as coherent, low-angle and high coincidence boundaries [58] may be

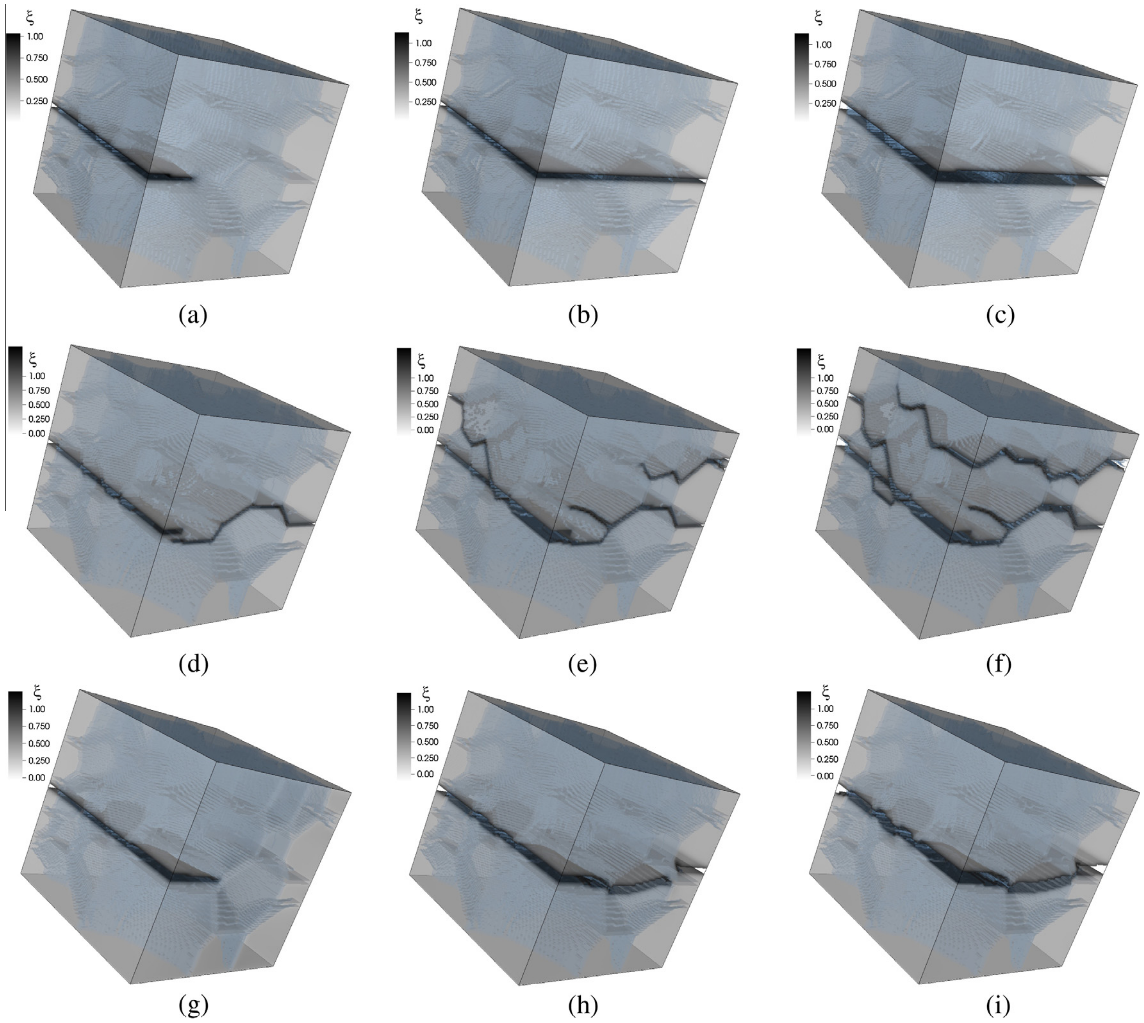

Fig. 2. Fracture profiles in elastically anisotropic SiC polycrystal (microstructure 1) for isotropic surface energy ($\beta = 0$), unit grain boundary stiffness ratio $R_\mu = 1$, domain size $L = 100$ μm, lattice orientation set 1, where elements with $\xi > 0.7$ are removed for visualization: (a) $R_\Gamma = 1, \varepsilon = 0.05\%$; (b) $R_\Gamma = 1, \varepsilon = 0.06\%$; (c) $R_\Gamma = 1, \varepsilon = 0.11\%$; (d) $R_\Gamma = 0.1, \varepsilon = 0.04\%$; (e) $R_\Gamma = 0.1, \varepsilon = 0.06\%$; (f) $R_\Gamma = 0.1, \varepsilon = 0.11\%$; (g) $R_\Gamma = 10, \varepsilon = 0.08\%$; (h) $R_\Gamma = 10, \varepsilon = 0.09\%$; (i) $R_\Gamma = 10, \varepsilon = 0.12\%$.

categorized as semi-coherent, and random high-angle boundaries with low coincidence are considered incoherent. Boundary surface energy (which may implicitly include short range elastic energy of defects) tends to increase with decreasing coherence. In most simulations reported herein, grains are assigned random initial lattice orientations, leading to high-angle boundaries that can be viewed as fully incoherent, though the statistical probability of a nonzero fraction of boundaries with low misorientation is not precluded. Each boundary is assigned the same surface energy regardless of misorientation. A more physically realistic approach might assign variable surface energy Γ dependent on misorientation or other geometric grain boundary characteristics, but such an approach (which necessarily involves introduction of more model parameters for prospective study) is not considered in this work. For some simulations in which grain boundary fractures are intentionally prohibited, surface energy of boundaries can be considered infinite, but cleavage fractures in the vicinity of and traversing across grain boundaries remain possible.

Tensile deformation boundary conditions are considered in Section 4, corresponding to an average state of uniaxial stress. Consider for example straining in the z-direction. Tensile displacement increments δu are prescribed along the face $z = L$, while lateral edges of the cube are left free to contract due to the Poisson effect. The cumulative average strain is $\varepsilon = \sum \delta u / L$, with summation over the number of applied strain increments. Upon application of each increment, a solution of the governing equations is found via conjugate gradient energy minimization, as discussed in Section 3.1. Each microstructure is seeded with an initial defect, specifically an edge crack, along the midplane $(L/2)$ of one edge of the cube and oriented perpendicular to the direction of loading, as shown in Fig. 1(d). The initial length and thickness of the crack, wherein conditions $\xi = 1$ are applied throughout the simulation, are $0.1L$ and $0.02L$. The initial crack traverses grains and grain boundary regions and tends to extend in mode I fashion when the applied tensile strain is sufficiently large.

4. Results and discussion

4.1. Effects of crystal and grain boundary properties

First examined are effects of grain boundary strength, as prescribed by R_Γ defined in (3.1). Shown in Fig. 2 are representative phase field simulation results for SiC polycrystals with $0.1 \leqslant R_\Gamma \leqslant 10$. For the case shown in Fig. 2(a)–(c) at successively larger applied strain ε, $R_\Gamma = 1$ and the only source of heterogeneity is elastic anisotropy among crystals. The initial edge crack

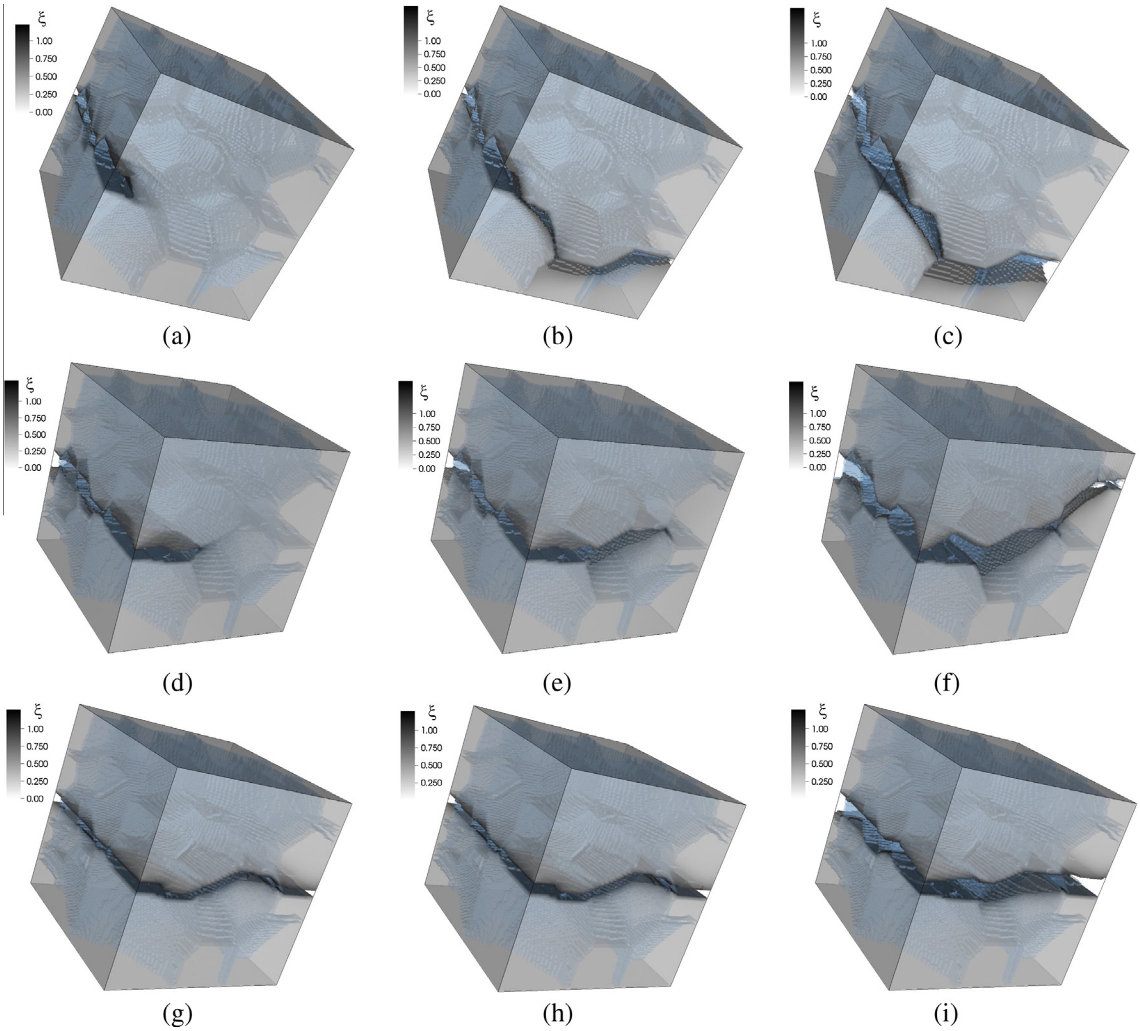

(a) (b) (c)
(d) (e) (f)
(g) (h) (i)

Fig. 3. Fracture profiles in elastically anisotropic SiC polycrystal (microstructure 1) for anisotropic surface energy ($\beta > 0$), unit grain boundary stiffness and energy ratios $R_\mu = R_\Gamma = 1$, domain size $L = 100$ µm, where elements with $\xi > 0.7$ are removed for visualization: (a) lattice orientation 1, $\beta = 100, \varepsilon = 0.07\%$; (b) lattice orientation 1, $\beta = 100, \varepsilon = 0.08\%$; (c) lattice orientation 1, $\beta = 100, \varepsilon = 0.16\%$; (d) lattice orientation 2, $\beta = 100, \varepsilon = 0.07\%$; (e) lattice orientation 2, $\beta = 100, \varepsilon = 0.08\%$; (f) lattice orientation 2, $\beta = 100, \varepsilon = 0.16\%$; (g) lattice orientation 2, $\beta = 10, \varepsilon = 0.07\%$; (h) lattice orientation 2, $\beta = 10, \varepsilon = 0.08\%$; (i) lattice orientation 2, $\beta = 10, \varepsilon = 0.11\%$.

propagates straight across the sample since fracture properties are uniform among grains and grain boundary regions. For the case shown in Fig. 2(d)–(f), $R_\Gamma = 0.1$, corresponding to weak amorphous regions at grain boundaries. Resulting fracture patterns are dominated by intergranular networks of cracks. For the case shown in Fig. 2(g)–(i), $R_\Gamma = 10$, corresponding to strong grain boundary phases and leading to predominantly transgranular crack networks, with crack blockage occurring at some grain boundaries. Similar trends were reported in [12], where the ratio of transgranular to intergranular fractures was predicted to increase with increasing R_Γ in 2D simulations of elastically isotropic polycrystals using XFEM.

Considered next are effects of cleavage energy anisotropy, as measured by nonzero values of β in (2.12). Recall that on a plane with unit normal $\boldsymbol{M}$, here corresponding to [0001] directions in a hexagonal lattice, surface energy is of base value Γ, while it increases by a factor of up to β on planes with orientations orthogonal to $\boldsymbol{M}$. Shown in Fig. 3 are results for which $R_\Gamma = 1$, meaning that intrinsically weak cleavage (i.e., basal) planes have strengths comparable to grain boundary facets, while other planes within each crystal have strengths effectively exceeding grain boundary strengths. Comparing two cases with different lattice orientation sets in Fig. 3(a)–(c) and (d)–(f), all with $\beta = 100$ [34], different fracture patterns emerge as a result of cleavage and elastic anisotropy, consisting of a mixture of transgranular and intergranular cracks. As shown in Fig. 3(g)–(i), decreasing β to 10 reduces the cleavage anisotropy, and the crack network becomes more transgranular in character relative to the cases with $\beta = 100$.

Studied next are effects of the thickness of the amorphous grain boundary phase in SiC polycrystals with anisotropic elasticity and anisotropic surface energy ($\beta = 100$). Results for microstructures 2 and 3 of Fig. 1 are depicted in Fig. 4(a)–(f), with two different initial lattice orientation distributions shown for microstructure 3. These results can be compared with those in Fig. 2(a)–(g) for microstructure 1. Recall from Section 3.3 and Table 3 that microstructure 1 contains the largest fraction of amorphous phase ($\upsilon \approx 20\%$), microstructure 2 somewhat less ($\upsilon \approx 14\%$) and microstructure 3 no amorphous phase ($\upsilon = 0$, perfectly bonded crystals). Inspection of the order parameter contours in Figs. 3(a)–(c) and 4(a)–(d) demonstrates that fracture patterns are similar, but not identical, in microstructures with different volume fractions of grain boundary regions but all with the same initial lattice orientation distribution.

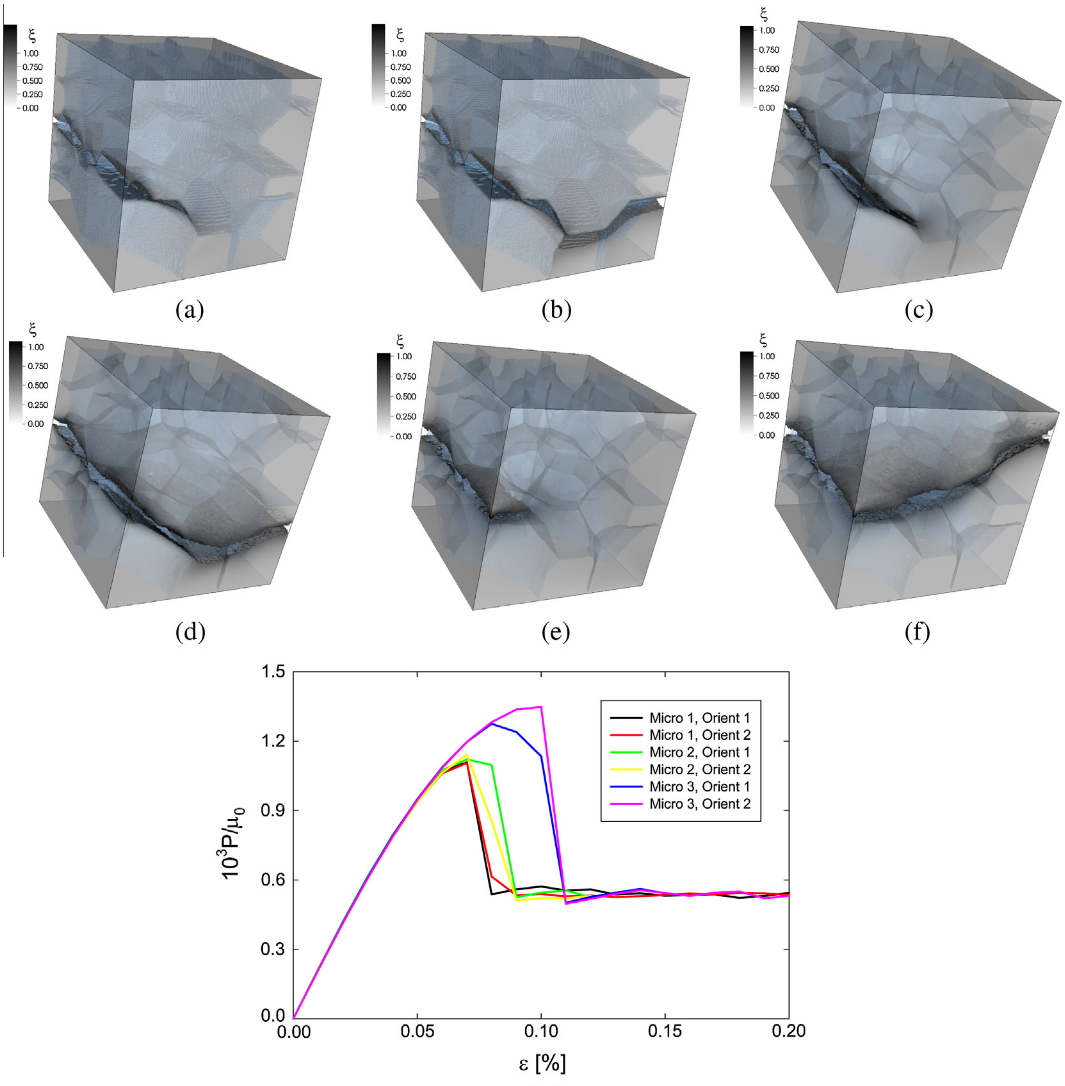

(a) (b) (c)

(d) (e) (f)

(g)

Fig. 4. Fracture profiles in elastically anisotropic SiC polycrystals for anisotropic surface energy ($\beta = 100$), unit grain boundary stiffness and energy ratios $R_\mu = R_\Gamma = 1$, domain size $L = 100$ μm, where elements with $\xi > 0.7$ are removed for visualization: (a) microstructure 2, lattice orientation 1, $\varepsilon = 0.08\%$; (b) microstructure 2, lattice orientation 1, $\varepsilon = 0.09\%$; (c) microstructure 3, lattice orientation 1, $\varepsilon = 0.09\%$; (d) microstructure 3, lattice orientation 1, $\varepsilon = 0.11\%$; (e) microstructure 3, lattice orientation 2, $\varepsilon = 0.10\%$; (f) microstructure 3, lattice orientation 2, $\varepsilon = 0.11\%$; (g) average axial stress versus applied axial strain.

Comparing Fig. 4(c) and (d) with Fig. 4(e) and (f) change in initial lattice orientation leads to different crack profiles in microstructure 3. Average stress–strain behavior is reported in Fig. 4(g), where P is the average normal component of stress tensor $\boldsymbol{P}$ in the entire specimen in the direction of loading. Peak strengths (i.e., maximum values of P) increase with decreasing volume fraction of grain boundary phase and are largest in microstructure 3. Such behavior is not unexpected since availability of weak regions to promote failure near grain boundaries should decrease with decreasing υ. Effects of lattice orientation on average tensile stress P are also apparent in Fig. 4(g) but are not as pronounced as effects of grain boundary microstructure.

Results in prior Figs. 2–4 all addressed SiC polycrystals with grain sizes d in the conventional regime ($L \approx 4d = 100$ μm). Considered in Fig. 5 are fracture morphologies and average stress–strain behavior of SiC polycrystals with grain sizes on the order of tens of nm, wherein effects of amorphous grain boundary phases have been reported as increasingly important in experiments [6]. In particular, effects of elastic stiffness of grain boundary phases relative to that of the bulk polycrystal are studied in microstructure 1 [imposed via R_μ of (3.1)], with anisotropic elastic and failure properties prescribed for the grains. Comparing Fig. 5(a) and (b) (stiff grain boundary regions) with Fig. 5(c) and (d) (soft grain boundary regions), variation of R_μ leads to different fracture

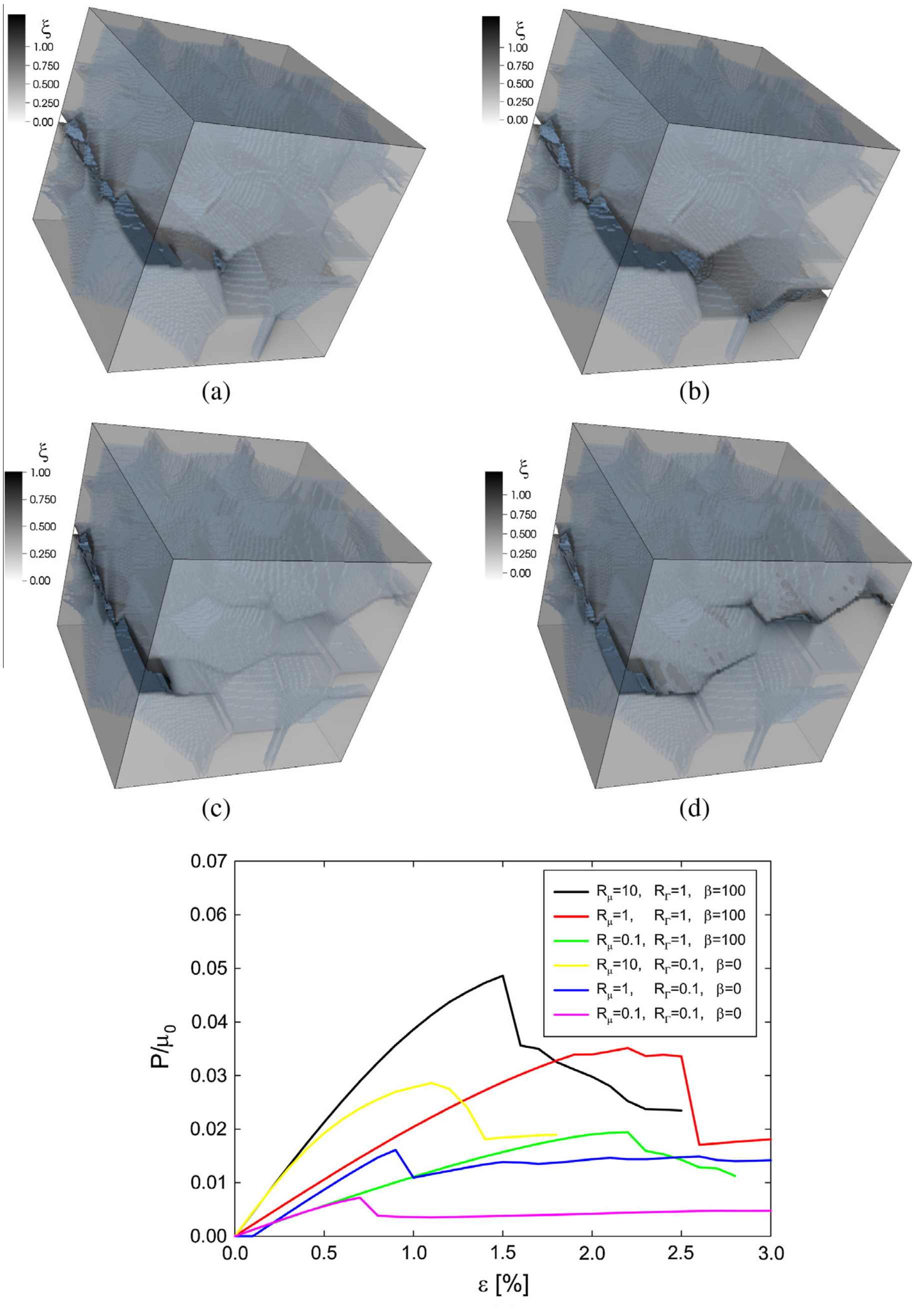

(a) (b) (c) (d) (e)

Fig. 5. Fracture profiles in elastically anisotropic SiC polycrystal (microstructure 1) for anisotropic surface energy ($\beta = 100$), unit grain boundary surface energy ratio $R_\Gamma = 1$, domain size $L = 100$ nm, lattice orientation set 1, where elements with $\xi > 0.7$ are removed for visualization: (a) $R_\mu = 10, \varepsilon = 1.8\%$ (b) $R_\mu = 10, \varepsilon = 2.2\%$ (c) $R_\mu = 0.1, \varepsilon = 2.1\%$ (d) $R_\mu = 0.1, \varepsilon = 2.8\%$; (e) average axial stress versus applied axial strain.

patterns, all a combination of cleavage and intergranular cracks. From average stress–strain behavior reported in Fig. 5(e), the following trends are apparent: initial tangent elastic modulus and peak strength increase with increasing R_μ, ductility does not necessarily increase with increasing R_μ, and peak strength decreases as grain boundary surface energy is reduced and cleavage anisotropy is eliminated ($R_\Gamma = 0.1$ and $\beta = 0$). Predicted trends for elastically compliant grain boundary phases are in general agreement with experiment [6]. As will be examined in more detail in Section 4.2, peak stress and ductility (i.e., ε at maximum P) are substantially larger for polycrystals with grain sizes on the order of tens of nm compared to those with sizes on the order of tens of microns, as is evident upon comparison of data in Figs. 4(g) and 5(e).

4.2. Effects of length scale

Representative results of phase field simulations for Zn polycrystals loaded in tension are shown in Fig. 6 for identical microstructures and properties except grain/domain size, which is set at $L = 100$ μm for results of Fig. 6 and $L = 100$ nm for results of Fig. 6(c) and (d). Fracture morphologies are remarkably similar regardless of length scale. However, applied tensile strains ε required to achieve the same state of overall damage are much larger for polycrystals with grain sizes on the order of nm than those with grain sizes on the order of μm. Peak loads are correspondingly larger for smaller specimens, as discussed more in what follows.

Critical average stress P_C (defined as the maximum average tensile stress attained prior to load drop associated with fracture propagation) is shown versus grain size d in Fig. 7(a) for Zn and SiC microstructures. In each data set, four grain sizes are considered, with material properties besides grain size (i.e., d, L, or l) held fixed. Initial lattice orientations and initial crack placements do vary among materials, however. Recall from Section 3.2 that l/L is fixed at 0.01 [47], such that variations in prescribed values of d and regularization width l are always directly proportional. In all cases, critical stress P_C increases with decreasing scale in an inverse square-root manner, i.e. $(P_C - P_0) \propto 1/\sqrt{d}$, with P_0 a constant limiting strength for very large grained structures. This trend is reminscent of Hall–Petch scaling observed in numerous metallic and ceramic polycrystals in the ultra-fine grained and nanocrystalline regimes [1–3]. Notice that the proportionality constant or slope of strength versus inverse root of size varies among materials and microstructures. For SiC with isotropic surface energy ($\beta = 0$), weakening the grain boundaries (decreasing R_Γ) decreases the slope or size effect. The same trend is obtained by holding R_Γ constant and decreasing β, which has the effect of decreasing the cleavage strength of many grains (depending on their orientation $\boldsymbol{M}$) relative to the grain boundary strength. It is also remarked that the present phase field predictions of critical strength proportional to $1/\sqrt{l}$ are in agreement with other phase field analyses of tensile fracture [32,47] and shear fracture [40] in homogeneous isotropic solids.

Table 4 reports ductility ε_C for SiC and Zn polycrystals of the same range of grain sizes considered in Fig. 7(a), with different random initial lattice orientations considered among the two materials and $\beta = 100$, $R_\Gamma = R_\mu = 1$. For each material data set, the following scaling relation is apparent:

$$\frac{(\varepsilon_C)_1}{(\varepsilon_C)_2} = \left(\frac{d_2}{d_1}\right)^{1/2}, \tag{4.1}$$

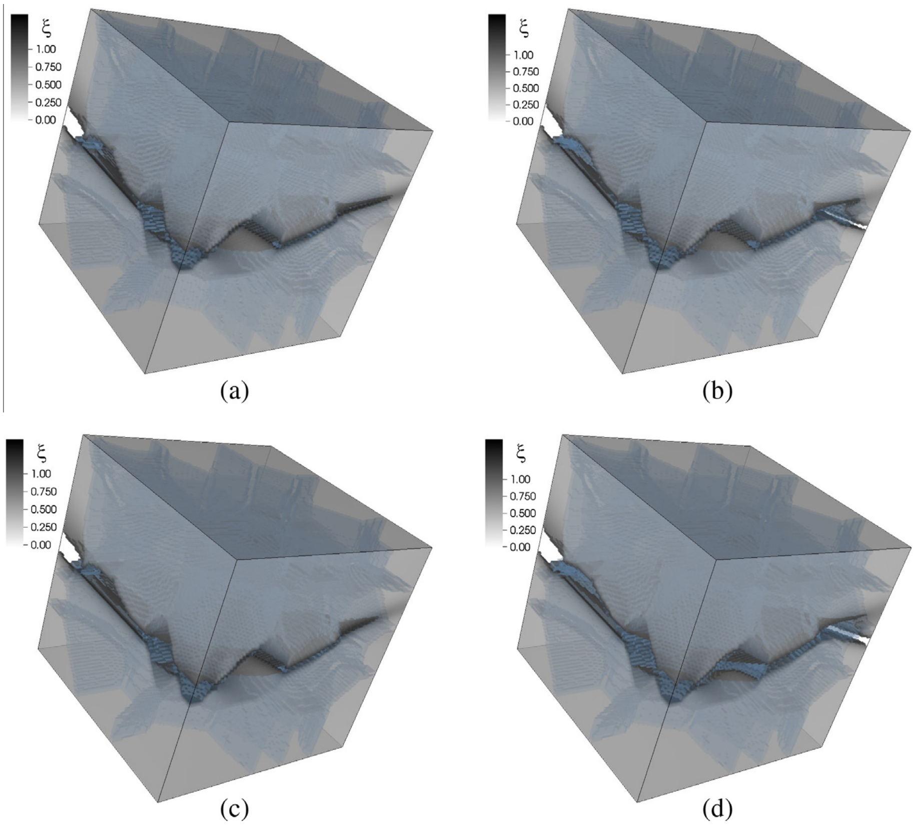

(a) (b)

(c) (d)

Fig. 6. Fracture profiles in elastically anistropic Zn polycrystal (microstructure 1) for anisotropic surface energy ($\beta = 100$), unit grain boundary stiffness and surface energy ratios $R_\mu = R_\Gamma = 1$, lattice orientation set 3, where elements with $\xi > 0.7$ are removed for visualization: (a) $L = 100\,\mu\text{m}, \varepsilon = 0.15\%$ (b) $L = 100\,\mu\text{m}, \varepsilon = 0.20\%$ (c) $L = 100\,\text{nm}, \varepsilon = 4.4\%$ (d) $L = 100\,\text{nm}, \varepsilon = 8.0\%$.

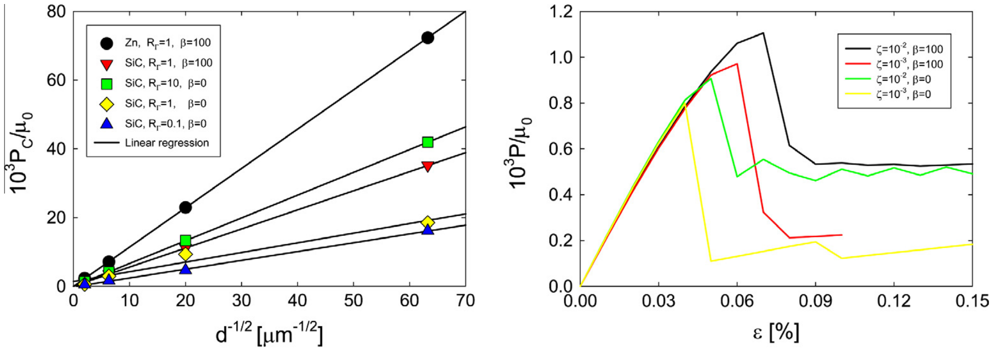

(a) (b)

Fig. 7. (a) Peak axial stress versus grain size *d* in Zn and SiC polycrystals and (b) average axial stress versus applied axial strain for various residual stiffness values ζ in SiC polycrystals.

Table 4
Polycrystalline ductility ε_C[%] versus grain size *d*.

Material	$d \approx 25$ μm	$d \approx 2.5$ μm	$d \approx 250$ nm	$d \approx 25$ nm
SiC	0.07	0.22	0.70	2.20
Zn	0.14	0.44	1.40	4.40

where subscripts 1 and 2 correspond to values for two different grain sizes. In other words, ductility, like strength, is predicted to increase with decreasing size in an inverse square root manner.

Finally, effects of residual strength parameter ζ are quantified in average stress–strain behavior shown in Fig. 7(b), results which correspond to SiC polycrystals with microstructure 1, lattice orientation set 1, and $L = 100$ μm. Peak strength and ductility increase slightly as ζ increases from 10^{-3} to 10^{-2}, while residual strength after the primary load drop increases significantly with increasing ζ. Numerical stability was found to increase with increasing ζ. Results for $\zeta = 10^{-4}$ (not shown) further confirmed these trends, which have also been noted in other phase field simulations [36] that considered values of $\zeta = 8 \times 10^{-4}$ and $\zeta = 8 \times 10^{-3}$. Results reported elsewhere in this paper have been obtained using $\zeta = 10^{-2}$, which produced the most numerically stable response; in such simulations, fully failed regions with $\xi \to 1$ have residual shear stiffness $\mu \to 0.01\mu_0$, which can be interpreted as very weakly elastic as opposed to pure free space with absolute zero stiffness.

5. Conclusions

Phase field theory and 3D finite element simulations of polycrystals–with individual crystals having anisotropic elastic coefficients and anisotropic fracture properties–have been described. Specifically studied materials include silicon carbide and zinc with hexagonal crystal structures and possibly intrinsically weak basal planes. In many simulations, second phases of isotropic amorphous material have been inserted in the vicinity of grain boundaries. Effects of the following microstructure characteristics and material properties on quasi-static tensile fracture have been investigated: initial lattice orientation; cleavage energy anisotropy; relative strength, stiffness, and thickness of grain boundary layers; and grain size (holding normalized regularization width fixed).

Key findings are summarized as follows. An increasing tendency for transgranular fracture has been observed as grain boundary surface energy increases or as cleavage plane anisotropy decreases. An increasing tangent modulus and increasing peak strength have been observed as elastic stiffness of the amorphous grain boundary phase increases. A decreasing peak strength has been predicted with increasing thickness or volume fraction of amorphous grain boundary phase. Finally, Hall–Petch scaling of peak tensile strength with variation in grain size has been observed, with the slope of the strength-size scaling relationship dependent on material properties.

References

[1] R.W. Rice, J. Mater. Sci. 32 (1997) 1673–1692.
[2] M.A. Meyers, A. Mishra, D.J. Benson, Prog. Mater. Sci. 51 (2006) 427–556.
[3] R.W. Armstrong, Acta Mech. 225 (2014) 1013–1028.
[4] H.D. Espinosa, P.D. Zavattieri, Mech. Mater. 35 (2003) 333–364.
[5] I. Szlufarska, A. Nakano, P. Vashishta, Science 309 (2005) 911–914.
[6] R.A. Andrievski, Rev. Adv. Mater. Sci. 22 (2009) 1–20.
[7] R.H. Kraft, J.F. Molinari, Acta Mater. 56 (2008) 4739–4749.
[8] J.W. Foulk, T.J. Vogler, Int. J. Fract. 163 (2010) 225–242.
[9] J.D. Clayton, R.H. Kraft, R.B. Leavy, Int. J. Solids Struct. 49 (2012) 2686–2702.
[10] X.-P. Xu, A. Needleman, Modell. Simul. Mater. Sci. Eng. 1 (1993) 111–132.
[11] J.D. Clayton, J. Mech. Phys. Solids 53 (2005) 261–301.
[12] N. Sukumar, D.J. Srolovitz, T.J. Baker, J.-H. Prevost, Int. J. Numer. Methods Eng. 56 (2003) 2015–2037.
[13] G.K. Sfantos, M.H. Aliabadi, Int. J. Numer. Methods Eng. 69 (2007) 1590–1626.
[14] T. Sadowski, S. Hardy, E. Postek, Mater. Sci. Eng. A 424 (2006) 230–238.
[15] V.A. Levitas, V.A. Levin, K.M. Zingerman, E.I. Freiman, Phys. Rev. Lett. 103 (2009) 025702.
[16] T. Hirouchi, T. Takaki, Y. Tomita, Comput. Mater. Sci. 44 (2009) 1192–1197.
[17] A. Hunter, I.J. Beyerlein, T.C. Germann, M. Koslowski, Phys. Rev. B 84 (2011) 144108.
[18] M.R. Tonks, D. Gaston, P.C. Millett, D. Andrs, P. Talbot, Comput. Mater. Sci. 51 (2012) 20–29.
[19] J.D. Clayton, J. Knap, Physica D 240 (2011) 841–858.
[20] J.D. Clayton, J. Knap, Modell. Simul. Mater. Sci. Eng. 19 (2011) 085005.
[21] T.W. Heo, Y. Wang, S. Bhattacharya, X. Sun, S. Hu, L.Q. Chen, Philos. Mag. Lett. 91 (2011) 110–121.
[22] J.D. Clayton, J. Knap, Acta Mater. 61 (2013) 5341–5353.
[23] R. Kondo, Y. Tadano, K. Shizawa, Comput. Mater. Sci. 95 (2014) 672–683.
[24] J.D. Clayton, AIMS Mater. Sci. 1 (2014) 143–158.
[25] Y.M. Jin, Y.U. Wang, A.G. Khachaturyan, Appl. Phys. Lett. 79 (2001) 3071–3073.
[26] V. Hakim, A. Karma, J. Mech. Phys. Solids 57 (2009) 342–368.
[27] C. Kuhn, R. Muller, Eng. Fract. Mech. 77 (2010) 3625–3634.
[28] C. Miehe, F. Welschinger, M. Hofacker, J. Mech. Phys. Solids 58 (2010) 1716–1740.
[29] C. Miehe, F. Welschinger, M. Hofacker, Int. J. Numer. Methods Eng. 83 (2010) 1273–1311.
[30] A. Abdollahi, I. Arias, Modell. Simul. Mater. Sci. Eng. 19 (2011) 074010.
[31] A. Abdollahi, I. Arias, Int. J. Fract. 174 (2012) 3–15.
[32] M.J. Borden, C.V. Verhoosel, M.A. Scott, T.J.R. Hughes, C.M. Landis, Comput. Methods Appl. Mech. Eng. 217 (2012) 77–95.
[33] G.Z. Voyiadjis, N. Mozaffari, Int. J. Solids Struct. 50 (2013) 3136–3151.
[34] J.D. Clayton, J. Knap, Int. J. Fract. 189 (2014) 139–148.
[35] B. Bourdin, G.A. Francfort, J.-J. Marigo, J. Mech. Phys. Solids 48 (2000) 797–826.
[36] G. Del Piero, G. Lancioni, R. March, J. Mech. Phys. Solids 55 (2007) 2513–2537.
[37] B. Bourdin, G.A. Francfort, J.-J. Marigo, J. Elasticity 91 (2008) 1–148.
[38] J.D. Clayton, Int. J. Impact Eng. 35 (2008) 269–289.
[39] J.D. Clayton, Int. J. Fract. 163 (2010) 151–172.
[40] J.D. Clayton, J. Knap, Nonlinear phase field theory for fracture and twinning with analysis of simple shear, Philos. Mag. (2015). submited for publication.
[41] C. Gandhi, M.F. Ashby, Acta Metall. 27 (1979) 1565–1602.
[42] J.C. Bielello, D. Dew-Hughes, A.T. Pucino, J. Appl. Phys. 54 (1983) 1821–1826.

[43] F. Chmelik, Z. Trojanova, P. Lukac, Z. Prevorovsky, J. Mater. Sci. Lett. 12 (1993) 1166–1168.
[44] X. Zhang, H. Wang, R.O. Scattergood, J. Narayan, C.C. Koch, A.V. Sergueeva, A.K. Mukherjee, Acta Mater. 50 (2002) 4823–4830.
[45] J.D. Clayton, Philos. Mag. 92 (2012) 2860–2893.
[46] J.D. Clayton, Int. J. Eng. Sci. 79 (2014) 1–20.
[47] H. Amor, J.-J. Marigo, C. Maurini, J. Mech. Phys. Solids 57 (2009) 1209–1229.
[48] J.D. Clayton, Nonlinear Mechanics of Crystals, Springer, Dordrecht, 2011.
[49] J.D. Clayton, K.M. Bliss, Mech. Mater. 68 (2014) 104–119.
[50] J.D. Clayton, J. Mech. Phys. Solids 61 (2013) 1983–2014.
[51] J.D. Clayton, Quart. J. Mech. Appl. Math. 67 (2014) 127–158.
[52] J.D. Clayton, J. Appl. Phys. 107 (2010) 013520.
[53] C.W. Garland, R. Dalven, Phys. Rev. 111 (1958) 1232–1234.
[54] J.J. Gilman, J. Appl. Phys. 31 (1960) 2208–2218.
[55] A.D. Rollett, S.B. Lee, R. Campman, G.S. Rohrer, Ann. Rev. Mater. Res. 37 (2007) 627–658.
[56] A.D. Rollett, P. Manohar, in: D. Raabe, F. Roters, F. Barlat, L-Q Chen (Eds.), Continuum Scale Simulation of Engineering Materials, Wiley-VCH, Weinheim, 2004, pp. 77–114.
[57] R.H. Kraft, I.S. Batyrev, S. Lee, A.D. Rollett, B. Rice, in: J. Swab (Ed.), Ceramic Eng. Sci. Proc. Adv. Ceramic Armor VI, Wiley, Hoboken NJ, 2010, pp. 143–158.
[58] D.G. Brandon, Acta Metall. 14 (1966) 1479–1484.
[59] P. Cermelli, M.E. Gurtin, Acta Metall. Mater. 42 (1994) 3349–3359.

1 (PDF)	DEFENSE TECHNICAL INFORMATION CTR DTIC OCA
2 (PDF)	DIRECTOR US ARMY RESEARCH LAB RDRL CIO LL IMAL HRA MAIL & RECORDS MGMT
1 (PDF)	GOVT PRINTG OFC A MALHOTRA
37 (PDF)	DIR USARL RDRL CIH C J KNAP RDRL WM B FORCH J MCCAULEY RDRL WML B I BATYREV B RICE D TAYLOR N WEINGARTEN RDRL WML H C MEYER B SCHUSTER RDRL WMM J BEATTY RDRL WMM B G GAZONAS D HOPKINS B POWERS RDRL WMM E J SWAB RDRL WMM F T SANO M TSCHOPP RDRL WMM G J ANDZELM RDRL WMP S SCHOENFELD RDRL WMP A S BILYK RDRL WMP B C HOPPEL S SATAPATHY M SCHEIDLER A SOKOLOW T WEERASOORIYA RDRL WMP C R BECKER T BJERKE D CASEM J CLAYTON D DANDEKAR M GREENFIELD R LEAVY J LLOYD S SEGLETES A TONGE C WILLIAMS RDRL WMP D R DONEY C RANDOW

INTENTIONALLY LEFT BLANK.